

Andreev Reflections in NbN/graphene Junctions under Large Magnetic Fields

Da Wang,^{†,‡,⊥} Evan J. Telford,^{†,⊥} Avishai Benyamini,^{†,‡} John Jesudasan,[¶]
Pratap Raychaudhuri,[¶] Kenji Watanabe,[§] Takashi Taniguchi,[§] James Hone,[‡]
Cory R. Dean,^{*,†} and Abhay N. Pasupathy^{*,†,||}

[†]*Department of Physics, Columbia University, New York, NY 10027, USA*

[‡]*Department of Mechanical Engineering, Columbia University, New York, NY 10027, USA*

[¶]*Tata Institute of Fundamental Research, Homi Bhabha Road, Colaba, Mumbai 400 005
India*

[§]*National Institute for Materials Science, 1-1 Namiki, Tsukuba, 305-0044 Japan*

^{||}*Condensed Matter Physics and Materials Science Department, Brookhaven National
Laboratory, Upton, NY 11973, USA*

[⊥]*These authors contributed equally to this work*

E-mail: cd2478@columbia.edu; apn2108@columbia.edu

Abstract

Hybrid superconductor/graphene (SC/g) junctions are excellent candidates for investigating correlations between Cooper pairs and quantum Hall (QH) edge modes. Experimental studies are challenging as Andreev reflections are extremely sensitive to junction disorder and high magnetic fields are required to form QH edge states. We fabricated low-resistance SC/g interfaces, composed of graphene edge contacted with NbN with a barrier strength of $Z \approx 0.4$, that remain superconducting under magnetic

fields larger than 18 T. We establish the role of graphene’s Dirac band structure on zero-field Andreev reflections and demonstrate dynamic tunability of the Andreev reflection spectrum by moving the boundary between specular and retro Andreev reflections with parallel magnetic fields. Through the application of perpendicular magnetic fields, we observe an oscillatory suppression of the 2-probe conductance in the $\nu = 4$ Landau level attributed to the reduced efficiency of Andreev processes at the NbN/g interface, consistent with theoretical predictions.

Keywords

two-dimensional, van der Waals, graphene, niobium nitride, superconductivity, Andreev reflection, quantum Hall effect, Zeeman splitting

Text

At the interface between a normal metal and a superconductor, electrons in the normal metal with energy below the superconducting gap can only transition into the superconductor via Andreev reflection, where an electron incident on the interface reflects as a hole along with the transmission of a Cooper pair into the superconductor. The probability of this process strongly depends on the band structure of the normal metal and the properties of the interface. Graphene, due to its Dirac band structure with a highly tunable Fermi level, is an enticing avenue to explore the role of the normal metal’s electronic properties on Andreev processes.¹⁻⁶ Initial experiments by Efetov in 2016 demonstrated the effect of graphene’s Dirac electronic structure on Andreev processes, identifying intraband Andreev processes (RAR) and interband Andreev processes (SAR). Under the application of perpendicular magnetic fields, graphene hosts chiral QH edge states, which has allowed for the investigation of Andreev process from integer QH states,⁶⁻⁹ which manifest non-Abelian zero modes of Majorana fermions.^{6,10-13} However, there are still many unanswered questions such as how

junction transparency and the proximity effect in graphene evolve under large perpendicular magnetic fields in the integer and fractional QH regime and the role of interfacial vortices on the junction properties. In addition the effect of large parallel magnetic fields on the Andreev reflection spectrum (where Zeeman splitting is induced without the formation of QH states) has thus far been unexplored. The limitations in experiments on SC/g junctions arise from technical challenges in fabricating SC/g junctions with favorable properties. Previous reports on SC/g junctions suffer either from relatively low junction transparency (as Andreev reflections are extremely sensitive to interfacial inhomogeneity and disorder^{14,15}) or low critical magnetic fields (≤ 8 T), limited by the superconducting contact.^{3,7}

In this paper, we report SC/g junctions fabricated using Niobium Nitride (NbN) as an edge contact to bilayer graphene fully encapsulated with hexagonal Boron Nitride (hBN).^{16,17} Bilayer graphene is used due to the smaller disorder broadening of the charge neutrality point (CNP) compared to monolayer graphene.²⁻⁴ Figure 1A shows the schematic of the device. First we use the dry-polymer-transfer technique to make a fully encapsulated graphene heterostructure,¹⁷ followed by electron beam (e-beam) lithography and reactive ion etching to define the device area. Superconducting (2 nm Ti + 100 nm NbN) and normal metal (2 nm Cr + 90 nm Au) edge contacts are patterned by e-beam lithography and deposited by e-beam deposition (Cr/Ti/Au) and sputtering (NbN).¹⁸ By sweeping the back-gate voltage and total current bias, we have full control of the Fermi energy in graphene and voltage bias across the NbN/g junction. NbN has a large, isotropic upper critical field¹⁹ (figure S1), which allows for the investigation of finite-field phenomena such as vortex formation at the NbN/g edge, junction transparency as a function of magnetic field, and the role of Zeeman splitting on Andreev reflections. By investigating the perpendicular magnetic field dependence of the junction resistance, we observe a suppression of the conductance within the QH plateaus, which can be well explained by interfacial scattering at a non-ideal SC/2DEG interface using the Blonder-Tinkham-Klapwijk (BTK) theory to model the scattering of QH edge states.^{20,21} Studying the junction under parallel magnetic fields, we observe shifts in

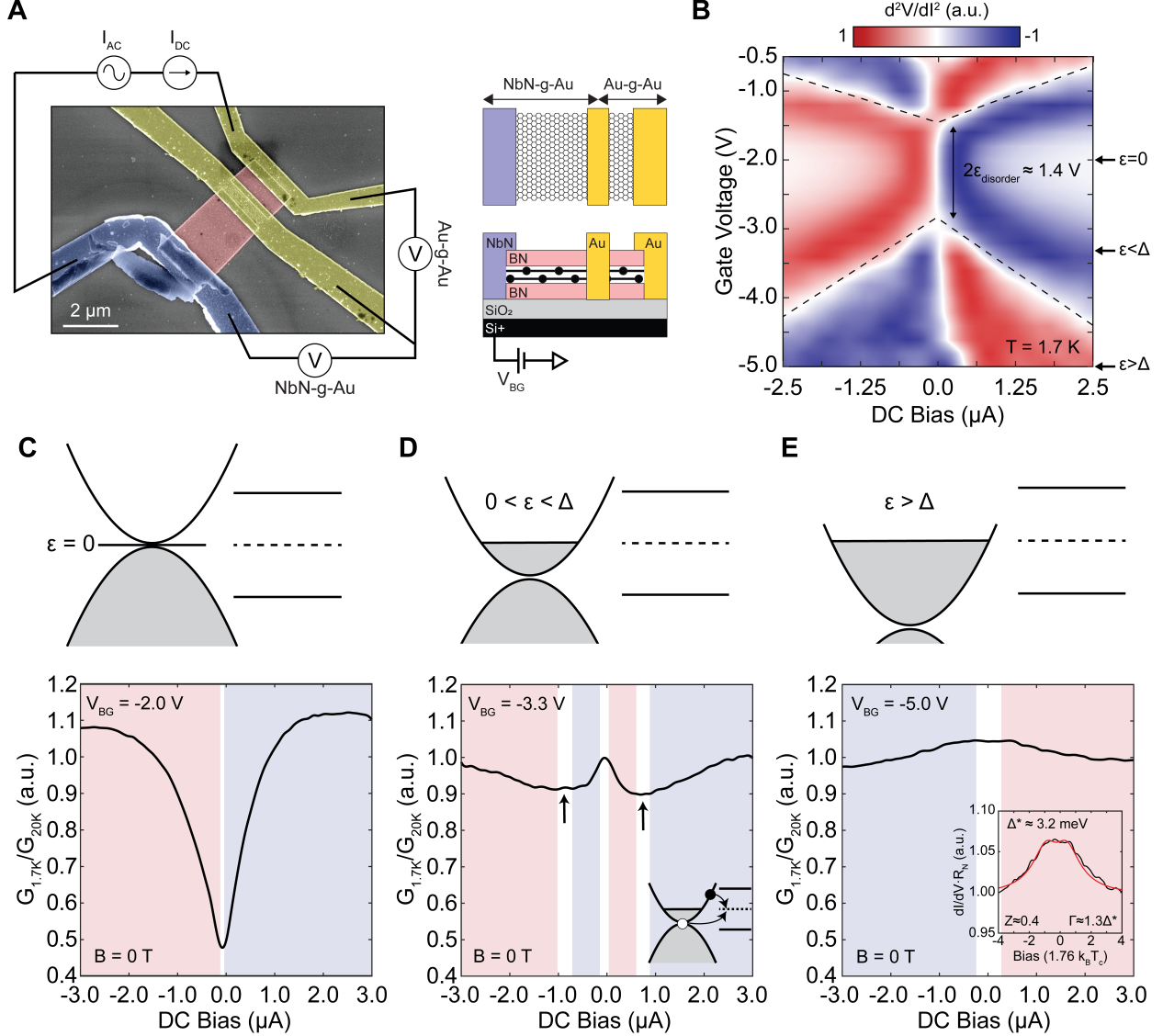


Figure 1: Andreev reflection in a NbN/g junction at zero magnetic field. (A) A scanning electron microscopy (SEM) image of the measured device with the corresponding measurement configuration (left) and a top and side view schematic of the device geometry (right). Color code: blue, NbN leads; yellow, Au leads; red, hBN; grey, SiO₂; black, Si. (B) Derivative of differential junction resistance versus DC current bias and back-gate voltage. The dashed black lines denote the crossover from SAR to RAR regimes. Arrows label the position in gate voltage of the cuts in C-E. (C-E) differential conductance versus DC current bias for $V_{BG} = -2.0 \text{ V}$ (C), $V_{BG} = -3.3 \text{ V}$ (D), and $V_{BG} = -5.0 \text{ V}$ (E). Blue, red, and white colored regions correspond to increasing, decreasing, and constant differential conductance, respectively, in panel (B). A cartoon of the band structure at the NbN/g interface is given above each plot. The left side of each cartoon is an energy versus momentum diagram of the graphene band structure, while the right side is an energy versus real space diagram of the NbN band structure. The inset of (D) shows a cartoon of the Andreev processes when $\epsilon_F = e|V_{NS}|$. The injected electron (black dot) and Andreev reflected hole (white dot) have an energy of $\epsilon_{e/h} = \epsilon_F \pm eV_{NS}$. The inset of (E) plots the normalized junction conductance (solid black line) versus DC voltage bias with a fit to the BTK model (solid red line). Extracted junction parameters are given in the inset. The extracted SC gap of NbN is larger than expected ($\Delta^* > \Delta = 1.76 \cdot k_B T_C \approx 2 \text{ meV}$) as the voltage bias is not entirely dropped across the NbN/g junction.

the Andreev reflection spectrum in graphene, which is explained by Zeeman splitting of the graphene band structure.

We begin by investigating Andreev reflections at the NbN/g interface through non-equilibrium conductivity measurements at zero magnetic field in figure 1 (see supplemental for measurement details). By varying the electronic density in the graphene through electrostatic gating, we can access three distinct tunneling regimes (demonstrated in figures 1C-E). In regime 1, the Fermi level of graphene is at the CNP (cartoon in figure 1C). The NbN/g junction conductance manifests a local minimum at zero bias due to the vanishing graphene density of state (DOS). As the DC current bias is increased, the conductance increases as charge carriers are injected at a finite energy above or below the CNP (figure 1C; temperature dependence in figure S2). In regime 2, the Fermi level of the graphene is tuned away from the CNP, but within the superconducting gap of the NbN (cartoon in figure 1D). We observe a peak in the differential conductance at zero bias which is attributed to Andreev processes as the feature is suppressed for $T > T_C$ (figure S3). We also observe local differential conductance minima when the Fermi level of graphene is equal to the voltage bias across the junction interface ($\epsilon_F = e|V_{NS}|$) (figure 1D).^{2,3} In regime 3, the Fermi level of graphene is further tuned away from the CNP and outside of the superconducting gap of NbN. We observe a zero-bias differential conductance peak due to Andreev reflections. We no longer observe minima in the differential conductance as the CNP is outside of the superconducting gap and the graphene behaves as a normal metal. In this regime, we can quantify the transparency of the junction using BTK theory (see supplemental for details).¹⁴ We find the barrier strength of our junction to be $Z \approx 0.4$ with a broadening parameter of $\Gamma \approx 1.3\Delta^*$, comparable to other reported SC/g junctions.^{2,7,22} The large value of the broadening parameter Γ may be due to NbN/g interface disorder created during fabrication, doping inhomogeneities, or external electromagnetic noise.

Figure 1B shows a two-dimensional (2D) colormap of the derivative of the differential resistance $\left(\frac{d^2V}{dI^2}\right)$ versus DC bias and back-gate voltage. This emphasizes the boundaries

between the three observed tunneling regimes. The dashed black lines in figure 1B clearly define the boundary between SAR and RAR as previously observed in NbSe₂/graphene junctions^{2,3} (see figure S4 for temperature dependence). In the absence of disorder, the boundary between Andreev reflection regimes should intersect at $\epsilon_F = e|V_{DC}| = 0$. In our junction, we observe a finite width at $V_{DC} = 0$ due to disorder in the graphene, which we estimate to be $V_{disorder} \approx 0.7$ V, similar to previously reported NbSe₂/graphene junctions.³

We next explore the effect of parallel magnetic field as it is predicted that Zeeman splitting of graphene's Dirac cones will lead to the observation of specular Andreev processes at zero DC bias.⁴ Figure 2A shows a schematic energy vs. momentum diagram of the NbN/g interface under an in-plane magnetic field. Zeeman splitting breaks the spin degeneracy, energetically separating the graphene bands into two copies with opposite spins (see figure S5 for details). The boundary defining the crossover between RAR and SAR processes shifts correspondingly (figure 2B). A regime of SAR (diamond-shaped blue region in figure 2B) appears at zero bias. In that regime, injected electrons with spin up in the valence band are reflected as holes with spin down in the conduction band.¹⁰ To illustrate the movement of the boundary between SAR and RAR, cuts of differential conductance versus DC bias at selected magnetic fields are shown in figure 2C. We choose a fixed back-gate voltage of $V_{BG} = -4.2$ V, where we clearly observe the SAR/RAR boundary at zero magnetic field (see figure S6 for cuts at additional back-gate values). At a parallel field of 4.5 T, the conductance enhancement due to Andreev reflections at zero bias decreases. When the parallel field is increased further to 9 T, the zero-bias conductance peak has transitioned into a conductance dip, indicating a transition from tunneling regime 2 (figure 1D) to tunneling regime 1 (figure 1C). At higher fields up to 18 T, only a conductance dip is observed near zero bias likely because the NbN superconducting gap is below the graphene Fermi level (figure S8). By plotting the derivative of the differential resistance $\left(\frac{d^2V}{dI^2}\right)$ versus DC bias and back-gate voltage (as in figure 1B) at different in-plane magnetic fields, one can extrapolate how the boundary between tunneling regime 1 and regime 2 moves as a function of in-plane field

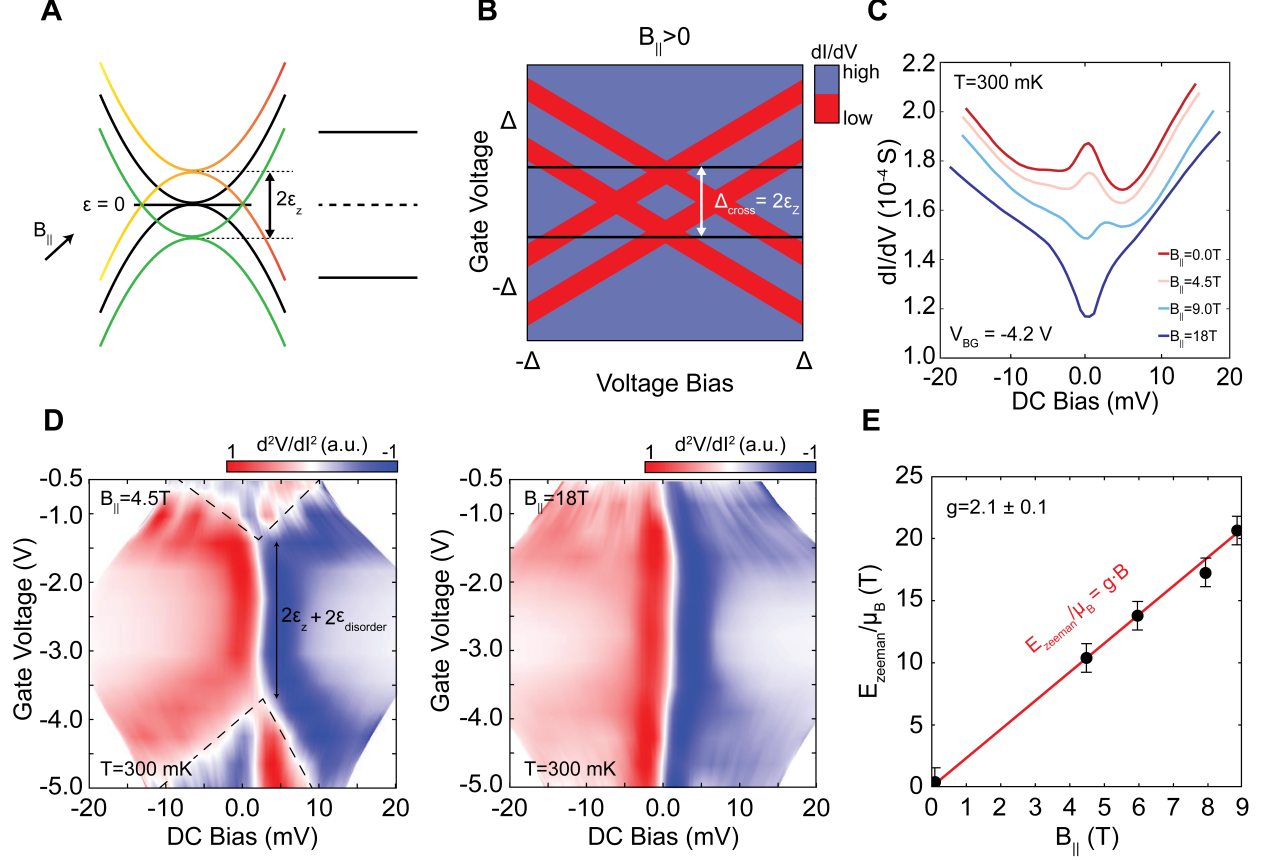


Figure 2: Andreev reflection in a NbN/g junction under parallel magnetic field. (A) Schematic diagram of energy vs. momentum at the NbN/g interface under an in-plane magnetic field. Zeeman splitting is denoted as ϵ_z . Unsplit bands are shown as solid black lines while spin up (down) bands are shown in orange (green). (B) Schematic of the anticipated differential conductance versus DC bias and back-gate voltage under an applied in-plane magnetic field. (C) Differential conductance versus DC voltage bias with $V_{BG} = -4.2$ V for various in-plane magnetic fields. (D) Colormap of the derivative of junction resistance ($\frac{d^2V}{dI^2}$) versus DC voltage bias and back-gate voltage at an in-plane magnetic field of 4.5 T (left) and 18 T (right). DC voltage bias was converted from DC current bias by integrating the measured differential resistance and using $V = I \cdot R$. The dashed black lines denote the boundary between SAR and RAR regimes. (E) Zeeman splitting extracted by measuring the boundary between SAR and RAR (dashed black line in (D)) versus in-plane magnetic field. The extracted g factor is $g = 2.1 \pm 0.1$.

(figure 2D and figure S7). We define the boundary between the two tunneling regimes as the V_{BG} at which a zero-bias conductance peak appears. With no disorder, one would expect the zero-bias conductance peaks to appear for any finite gate bias away from the CNP (with $\epsilon_F < \Delta$). The role of disorder is to broaden the CNP so the zero-bias conductance peaks appear at finite gate biases away from the CNP. We assume the broadening is independent of magnetic field, so any changes in the position of the boundary relative to the zero-field position is attributed to Zeeman splitting. In figure 2D, the boundary has moved from $V_{BG} = -3.4$ V (at zero field, figure S7) to $V_{BG} = -3.8$ V at 4.5 T (figure 2D left) and disappears completely at 18 T (figure 2D right). By tracking the position of the boundary for different in-plane magnetic fields, we extract the induced Zeeman splitting (figure 2E). The induced Zeeman splitting is linear with the applied field and we extract an effective g factor of $g = 2.1 \pm 0.1$.

By applying perpendicular magnetic fields, we can investigate correlations between superconductivity and the QHE. In the QH regime, the bulk conductance of graphene vanishes, and electrons are only transported through edge conductance channels. A semi-classical skipping orbit picture can be used to understand the Andreev process that occur at the NbN/g interface (figure 3A). Electrons are injected at one edge of the interface and reflected as holes (green) as a result of intraband RAR process. Through a similar Andreev process, the reflected holes are re-reflected as electrons at the NbN/g interface. For long junction widths ($W \gg R_C$, where W is the junction width and R_C is the cyclotron radius), an equilibrium superposition of electrons and holes is formed at the SC/g interface known as an Andreev bound state. As Schön et al. pointed out, the Büttiker description of quantum transport can be used to calculate the Andreev contribution to the conductance at a SC/2DEG interface in the QH regime.

$$G_{AR} = \frac{e^2}{\pi\hbar} \sum_1^{n^*} B_n \quad (1)$$

B_n is the hole probability for a particular Andreev bound state and the summation is over

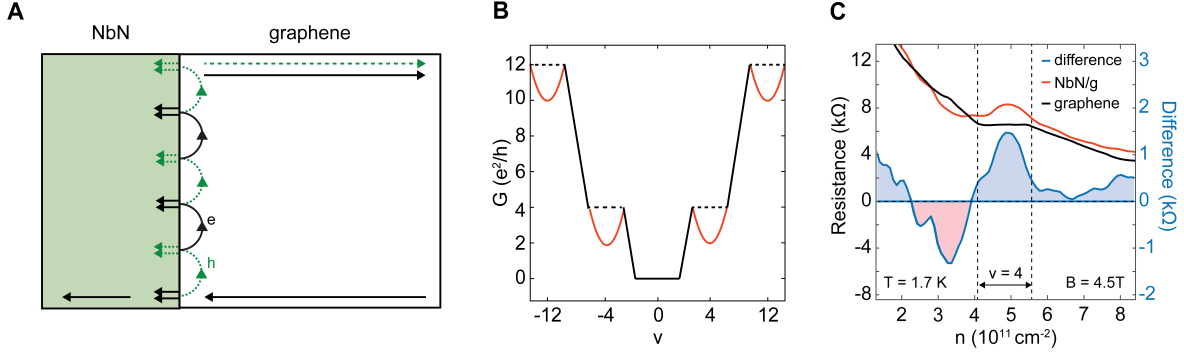


Figure 3: Intersection of the QHE and superconductivity. (A) A schematic of the classical skipping orbit picture at the NbN/g interface. Electron (hole) trajectories are given by solid black (green dashed) lines. NbN and graphene are denoted by green and grey regions, respectively. (B) Schematic of conductance versus filling factor for a SC/g junction in the QH regime with a perfect interface transparency $w = 0$ (solid and dashed black line) and a non-ideal interface transparency $w > 0$ (solid black line and solid red line).²⁰ (C) graphene channel (solid black curve) and NbN/g (solid red curve) junction resistance versus electron density measured at a perpendicular magnetic field of 4.5 T. In each curve, the contact resistance was extracted at zero field at a graphene carrier density of $n \approx 2.4 \times 10^{12} \text{ cm}^{-2}$ and subtracted from the presented data. The difference between the two curves is given by the solid blue curve. Highlighted blue and red regions signify when the NbN/g junction resistance is larger and smaller than the graphene channel (Au/g) resistance, respectively. The vertical dashed black lines demarcate the $\nu = 4$ plateau.

the Andreev bound states that intersect with the chemical potential.²⁰ The energy spectrum of Andreev bound states (and hole probabilities B_n) at the SC/2DEG interface is found by solving the Bogoliubov-de-Gennes (BdG) equation with spatially non-uniform single-electron/hole Hamiltonians and pair potential.²⁰ For an ideal interface without scattering, QH plateaus are predicted (figure 3B). For a non-ideal interface, we expect an oscillation of the conductance within a given Landau level (figure 3B).

To properly quantify the role of Andreev processes in the QH regime, we compare measurements of the NbN/g and graphene channel resistances versus Landau level filling factor for the same device (figure 3C). Contact resistances of $\approx 246\Omega$ for the NbN/g junction and $\approx 104\Omega$ for the Au/g junction were measured at a graphene carrier density of $n \approx 2.4 \times 10^{12} \text{ cm}^{-2}$ at zero magnetic field and zero DC bias. The contact resistances increase with magnetic field, but the difference in contact resistance between Au/g and NbN/g is nearly constant versus field (figure S9). Outside of the QH plateaus, the NbN/g and graphene channel dis-

play a nearly constant difference related to the discrepancy in contact resistance between Au and NbN for a given magnetic field. When graphene is tuned to the $\nu = 4$ QH state, the difference in conductance between graphene channel and NbN/g channel is prominent and depends upon carrier density in an oscillatory fashion. We can understand these observations by noting that Andreev processes are sensitive to the band structure of graphene.²⁰ Outside of the QH plateaus, conductance is dominated by bulk transport in which normal Andreev processes occur, whereas inside the QH plateaus, the only available Andreev process is through the Andreev bound edge states (figure 3A).

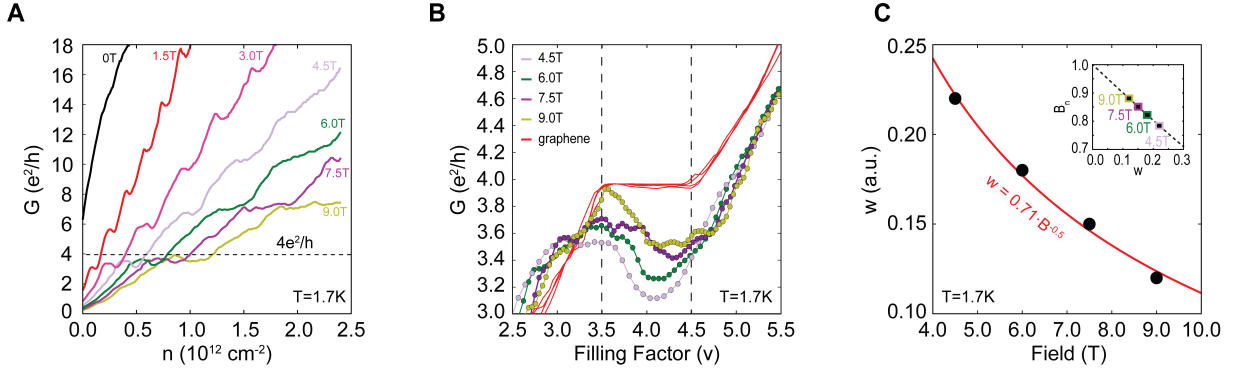


Figure 4: NbN/g junction transparency vs. perpendicular magnetic field. (A) NbN/g junction conductance versus graphene carrier density for various perpendicular magnetic field values. The $\nu = 4$ plateau is marked by a black dashed line. (B) NbN/g (yellow, purple, pink, and green solid lines) and graphene channel (red lines) conductance versus graphene filling factor at various perpendicular magnetic fields. The $\nu = 4$ plateau is marked by the black dashed lines. (C) Extracted scattering parameter w versus perpendicular magnetic field. The solid red line is a fit to the theoretically predicated $w \propto \frac{1}{\sqrt{B}}$ dependence. Inset: Extracted hole probability amplitude versus scattering parameter w for the data in (B). The dashed black line is a fit to the data with equation 2.

In figure 4, we characterize the quality of the NbN/g junction by examining the perpendicular magnetic field dependence of the junction conductance. In figure 4A, we plot the NbN/g junction conductance versus graphene carrier density at various perpendicular magnetic field values. The QH plateaus are not perfectly quantized (compared to our graphene channel in figure S10), which indicates a finite junction transparency. For analysis of the NbN/g junction quality, we focus on the $\nu = 4$ plateau as it is well developed in the graphene channel for all presented magnetic field values (figure 4B). From Schön et.al, the two impor-

tant parameters used to describe the quality of the junction are the Fermi velocity mismatch $s = \sqrt{\frac{\epsilon_F^S m_N}{\epsilon_F^N m_S}}$ (where ϵ_F^S , ϵ_F^N and m_S , m_N are the Fermi energies and effective electron masses for the superconductor and normal metal respectively) and the interfacial barrier strength $w = \sqrt{\frac{2m_N U_0^2}{\hbar^2 \epsilon_F^N}}$ (where U_0 is the interface scattering potential), which quantifies the interface scattering. For an ideal interface without backscattering and no Fermi velocity mismatch, $s = 1$, $w = 0$. For simplicity, we set $s = 1$ since it is magnetic field independent and our primary objective is to determine the magnetic field dependence of w . The barrier strength w can be determined by extracting the minimal NbN/g junction conductance within the $\nu = 4$ plateau region as the junction conductance depends only on w and ν .

$$G_{AR} = \frac{e^2}{\pi \hbar} \sum_1^4 B_n = 2 \frac{e^2}{\pi \hbar} \frac{q^2 / (1 - \gamma_0^2)}{(1 + \sqrt{1 - q^2 / (1 - \gamma_0^2)})} \quad (2)$$

$$q = \frac{2s}{s^2 + w^2 + 1} \quad (3)$$

$$\gamma_0 = \frac{(s^2 + w^2 - 1) \sin(\pi\nu/2) + 2w \cos(\pi\nu/2)}{s^2 + w^2 + 1} \quad (4)$$

The scattering parameter w depends upon magnetic field through $w = \sqrt{\frac{2m_N U_0^2}{\hbar^2 \epsilon_F^N(B)}}$, where $\epsilon_F^N(B) = \nu \frac{\hbar \omega_C}{2}$ and $\omega_C = \frac{eB}{mc}$ (figure S11). The inset of figure 4C shows extracted hole probability B_n versus scattering parameter w . We find w equals 0.22, 0.18, 0.15, 0.12 for perpendicular field values of $B = 4.5$ T, 6.0 T, 7.5 T, 9.0 T, respectively. We can demonstrate the data is well described by Schön's model²⁰ by fitting the extracted w versus magnetic field and comparing it to the expected $w \propto \frac{1}{\sqrt{B}}$ dependence. We find close agreement between our experiment and theory (figure 4C).

Although Schön's model²⁰ fits our data, it omits the contribution of higher order corrections to the conductance due to phase coherence in wide SC/2DEG junctions (defined as $W \gg R_C$, where W is the junction width and R_C is the cyclotron radius). It is worth discussing the role of phase coherence and why our data can be accurately described by the first order coherence term. When examining the SC/2DEG interface, the four tunneling

processes we consider are $e \rightarrow e$, $e \rightarrow h$, $h \rightarrow e$, $h \rightarrow h$, whose corresponding probabilities are $(r_{ee}, r_{eh}, r_{he}, r_{hh})$. To take phase coherence into consideration, the transmission matrix is generalized to include the spatial dependence of the superconductor phase $\phi(y)$ and to consider all possible scattering trajectories (in the form of individual action terms for electrons S_e and holes S_h).²³ The final expression for junction conductance can be written as

$$G(\nu) = \sum_{n=0}^{\infty} g_n \cos(2\pi\nu n + \delta_n) \quad (5)$$

where δ_n is related to the phase coherence. The higher order harmonics (n^{th} term corresponding to n coherent e/h bounces) are relevant for larger junction widths but are suppressed by the presence of interfacial disorder. The leading term to the conductance can be written:

$$G(\nu) \approx g_0 + g_1 \cos(2\pi\nu + \delta_1) \quad (6)$$

An intuitive way to understand the suppression of higher order terms by interface disorder is the following: at the junction, short range disorder is considered by introducing fluctuations that re-scatter electrons and holes, destroying phase coherence between multiple bounces. Therefore the conductance oscillations are predominantly described by the first order harmonic (approximation used in Schön's model²⁰) when the average length scale of the interface disorder and inhomogeneity is less than the cyclotron radius $R_C = \hbar k_F / 2\pi e B$.

In conclusion, low-resistance junctions between NbN, a superconductor with an isotropic critical magnetic field exceeding 18 T, and bilayer graphene are fabricated and investigated. At zero field, we observe the role of graphene's Dirac cones on Andreev reflections, demonstrating 3 distinct tunneling regimes. With the application of parallel fields, we demonstrate dynamic tunability of the boundary between RAR and SAR. The movement of the boundary corresponds to the expected Zeeman splitting in bilayer graphene, from which we extract a g factor of $g \approx 2.1 \pm 0.1$. Finally, through the application of perpendicular fields, we observe an oscillatory suppression of the 2-probe conductance in the $\nu = 4$ Landau level that is well

described by a theoretical model given by Schön et al.²⁰ For future experiments, realizing NbN/g junctions with lower graphene disorder broadening will allow us to better explore the regime of zero-field SAR near the CNP and investigate the intersection of superconductivity and the FQHE. Furthermore, if $\nu = 0$ helical edge modes in graphene are stabilized,^{24,25} counter propagating edge modes of quantum spin hall states can be realized at the NbN/g interface, which is predicted to host non-abelian Majorana physics.²⁵⁻²⁹

Supporting Information

The following files are available free of charge.

Fabrication Methods, Transport Measurements, Fitting Zero-Field NbN/g/Au Junction Conductance to BTK Theory, Modeling NbN/g/Au Junction Conductance in the QH Regime, Supporting Figures S1-S12 (PDF)

Corresponding Author

*Abhay N. Pasupathy (e-mail: apn2108@columbia.edu)

*Cory R. Dean (e-mail: cd2478@columbia.edu)

Notes

the authors declare no competing financial interests.

Author Contributions

The manuscript was written through contributions of all authors. All authors have given approval to the final version of the manuscript.

DW and EJT contributed equally

Funding Sources

This research was supported by the Columbia MRSEC on Precision-Assembled Quantum Materials (PAQM) - DMR-2011738, Honda Research Institute USA Inc and the Air Force Office of Scientific Research via grant FA9550-21-1-0378. A portion of this work was performed at the National High Magnetic Field Laboratory, which is supported by National Science Foundation Cooperative Agreement No. DMR-1157490 and the State of Florida. This work was performed in part at the Advanced Science Research Center NanoFabrication Facility of the Graduate Center at the City University of New York. The authors from TIFR would like to thank Department of Atomic Energy, Government of India (Grant No. 12-R&D-TFR-5.10-0100) for financial support.

Abbreviations

SC, superconductor; g, graphene; QH, quantum Hall; NbN, Niobium Nitride; SAR, specular Andreev reflection; RAR, retro Andreev reflection; FQHE, fractional quantum Hall effect; hBN, hexagonal Boron Nitride; CNP, charge neutrality point; e-beam, electron beam; BTK, Blonder-Tinkham-Klapwijk; DOS, density of states; 2D, two-dimensional; DC, direct current; AC, alternating current; QHE, quantum Hall effect; 2DEG, two-dimensional electron gas; BdG, Bogoliubov-de-Gennes

References

- (1) Beenakker, C. W. Specular andreev reflection in graphene. *Physical Review Letters* **2006**, *97*, 067007.
- (2) Efetov, D. K.; Efetov, K. B. Crossover from retro to specular Andreev reflections in bilayer graphene. *Physical Review B* **2016**, *94*, 075403.
- (3) Efetov, D. K.; Wang, L.; Handschin, C.; Efetov, K. B.; Shuang, J.; Cava, R.; Taniguchi, T.; Watanabe, K.; Hone, J.; Dean, C. R.; Kim, P. Specular interband Andreev reflections at van der Waals interfaces between graphene and NbSe₂. *Nature Physics* **2016**, *12*, 328–332.
- (4) Soori, A.; Sahu, M. R.; Das, A.; Mukerjee, S. Enhanced specular Andreev reflection in bilayer graphene. *Physical Review B* **2018**, *98*, 075301.
- (5) Sahu, M. R.; Raychaudhuri, P.; Das, A. Andreev reflection near the Dirac point at the graphene- NbSe₂ junction. *Physical Review B* **2016**, *94*, 235451.
- (6) Sahu, M. R.; Liu, X.; Paul, A. K.; Das, S.; Raychaudhuri, P.; Jain, J. K.; Das, A. Inter-Landau-level Andreev Reflection at the Dirac Point in a Graphene Quantum Hall State Coupled to a NbSe₂ Superconductor. *Physical Review Letters* **2018**, *121*, 086809.
- (7) Amet, F.; Ke, C. T.; Borzenets, I. V.; Wang, J.; Watanabe, K.; Taniguchi, T.; Deacon, R. S.; Yamamoto, M.; Bomze, Y.; Tarucha, S.; Finkelstein, G. Supercurrent in the quantum Hall regime. *Science* **2016**, *352*, 966–969.
- (8) Calado, V. E.; Goswami, S.; Nanda, G.; Diez, M.; Akhmerov, A. R.; Watanabe, K.; Taniguchi, T.; Klapwijk, T. M.; Vandersypen, L. M. Ballistic Josephson junctions in edge-contacted graphene. *Nature Nanotechnology* **2015**, *10*, 761–764.
- (9) Günel, H. Y.; Borgwardt, N.; Batov, I. E.; Hardtdegen, H.; Sladek, K.; Panaitov, G.; Grützmacher, D.; Schäpers, T. Crossover from josephson effect to single interface an-

- dreev reflection in asymmetric superconductor/nanowire junctions. *Nano Letters* **2014**, *14*, 4977–4981.
- (10) Lutchyn, R. M.; Sau, J. D.; Das Sarma, S. Majorana fermions and a topological phase transition in semiconductor-superconductor heterostructures. *Physical Review Letters* **2010**, *105*, 077001.
- (11) Sarma, S. D.; Freedman, M.; Nayak, C. Majorana zero modes and topological quantum computation. *npj Quantum Information* **2015**, *1*, 1–13.
- (12) San-Jose, P.; Lado, J. L.; Aguado, R.; Guinea, F.; Fernández-Rossier, J. Majorana zero modes in graphene. *Physical Review X* **2015**, *5*, 041042.
- (13) Fu, L.; Kane, C. L. Superconducting proximity effect and majorana fermions at the surface of a topological insulator. *Physical Review Letters* **2008**, *100*, 096407.
- (14) Blonder, G. E.; Tinkham, M.; Klapwijk, T. M. Transition from metallic to tunneling regimes in superconducting microconstrictions: Excess current, charge imbalance, and supercurrent conversion. *Physical Review B* **1982**, *25*, 4515–4532.
- (15) Daghero, D.; Gonnelli, R. S. Probing multiband superconductivity by point-contact spectroscopy. *Superconducting Science and Technology* **2010**, *23*, 43001–37.
- (16) Dean, C. R.; Young, A. F.; Meric, I.; Lee, C.; Wang, L.; Sorgenfrei, S.; Watanabe, K.; Taniguchi, T.; Kim, P.; Shepard, K. L.; Hone, J. Boron nitride substrates for high-quality graphene electronics. *Nature Nanotechnology* **2010**, *5*, 722–726.
- (17) Wang, L.; Meric, I.; Huang, P. Y.; Gao, Q.; Gao, Y.; Tran, H.; Taniguchi, T.; Watanabe, K.; Campos, L. M.; Muller, D. A.; Guo, J.; Kim, P.; Hone, J.; Shepard, K. L.; Dean, C. R. One-dimensional electrical contact to a two-dimensional material. *Science* **2013**, *342*, 614–617.

- (18) Chockalingam, S. P.; Chand, M.; Jesudasan, J.; Tripathi, V.; Raychaudhuri, P. Superconducting properties and Hall effect of epitaxial NbN thin films. *Physical Review B* **2008**, *77*, 214503.
- (19) Mondal, M.; Chand, M.; Kamlapure, A.; Jesudasan, J.; Bagwe, V. C.; Kumar, S.; Saraswat, G.; Tripathi, V.; Raychaudhuri, P. Phase diagram and upper critical field of homogeneously disordered epitaxial 3-dimensional NbN films. *Journal of Superconductivity and Novel Magnetism* **2011**, *24*, 341–344.
- (20) Hoppe, H.; Zülicke, U.; Schön, G. Andreev reflection in strong magnetic fields. *Physical Review Letters* **2000**, *84*, 1804–1807.
- (21) Eroms, J.; Weiss, D.; De Boeck, J.; Borghs, G.; Zülicke, U. Andreev reflection at high magnetic fields: Evidence for electron and hole transport in edge states. *Physical Review Letters* **2005**, *95*, 107001.
- (22) Lee, G. H.; Huang, K. F.; Efetov, D. K.; Wei, D. S.; Hart, S.; Taniguchi, T.; Watanabe, K.; Yacoby, A.; Kim, P. Inducing superconducting correlation in quantum Hall edge states. *Nature Physics* **2017**, *13*, 693–698.
- (23) Chtchelkatchev, N. M.; Burmistrov, I. S. Conductance oscillations with magnetic field of a two-dimensional electron gas-superconductor junction. *Physical Review B* **2007**, *75*, 214510.
- (24) Maher, P.; Dean, C. R.; Young, A. F.; Taniguchi, T.; Watanabe, K.; Shepard, K. L.; Hone, J.; Kim, P. Evidence for a spin phase transition at charge neutrality in bilayer graphene. *Nature Physics* **2013**, *9*, 154–158.
- (25) Young, A. F.; Sanchez-Yamagishi, J. D.; Hunt, B.; Choi, S. H.; Watanabe, K.; Taniguchi, T.; Ashoori, R. C.; Jarillo-Herrero, P. Tunable symmetry breaking and helical edge transport in a graphene quantum spin Hall state. *Nature* **2014**, *505*, 528–532.

- (26) Hart, S.; Ren, H.; Wagner, T.; Leubner, P.; Mühlbauer, M.; Brüne, C.; Buhmann, H.; Molenkamp, L. W.; Yacoby, A. Induced superconductivity in the quantum spin Hall edge. *Nature Physics* **2014**, *10*, 638–643.
- (27) Qi, X. L.; Zhang, S. C. Topological insulators and superconductors. *Reviews of Modern Physics* **2011**, *83*, 1057.
- (28) Wiedenmann, J.; Bocquillon, E.; Deacon, R. S.; Hartinger, S.; Herrmann, O.; Klapwijk, T. M.; Maier, L.; Ames, C.; Brüne, C.; Gould, C.; Oiwa, A.; Ishibashi, K.; Tarucha, S.; Buhmann, H.; Molenkamp, L. W. 4π -periodic Josephson supercurrent in HgTe-based topological Josephson junctions. *Nature Communications* **2016**, *7*, 1–7.
- (29) Bocquillon, E.; Deacon, R. S.; Wiedenmann, J.; Leubner, P.; Klapwijk, T. M.; Brüne, C.; Ishibashi, K.; Buhmann, H.; Molenkamp, L. W. Gapless Andreev bound states in the quantum spin Hall insulator HgTe. *Nature Nanotechnology* **2017**, *12*, 137–143.

Supplemental Materials

Andreev Reflections in NbN/graphene Junctions under Large Magnetic Fields

Da Wang,^{†,‡,⊥} Evan J. Telford,^{†,⊥} Avishai Benyamini,^{†,‡} John Jesudasan,[¶] Pratap Raychaudhuri,[¶] Kenji Watanabe,[§] Takashi Taniguchi,[§] James Hone,[‡] Cory R. Dean,^{*,†} and Abhay N. Pasupathy^{*,†,||}

†Department of Physics, Columbia University, New York, NY 10027, USA

‡Department of Mechanical Engineering, Columbia University, New York, NY 10027, USA

¶Tata Institute of Fundamental Research, Homi Bhabha Road, Colaba, Mumbai 400 005 India

§National Institute for Materials Science, 1-1 Namiki, Tsukuba, 305-0044 Japan

|| Condensed Matter Physics and Materials Science Department, Brookhaven National Laboratory, Upton, NY 11973, USA

⊥These authors contributed equally to this work

Fabrication Methods:

The graphene Hall bar was shaped using an Oxford Plasmalab 100 ICP-RIE with a $\text{CHF}_3:\text{O}_2$ 40:4 sccm gas mixture with 60 W RF power and 40 mTorr gas pressure. Standard electron beam lithography techniques were used to define the contact geometry. Normal metal electrodes (Cr + Au 2 nm + 90 nm) were deposited using standard electron beam deposition techniques.

Thin films of NbN were synthesized through reactive dc magnetron sputtering by sputtering a Nb target in Ar- N_2 gas mixture. The substrate temperature is kept at 100 °C, with an ambient pressure of 7 mTorr, and a target-to-substrate distance of 6.2 cm at a power of 220 W. The thickness of the NbN film is about 70-100 nm. The test sample films are grown on SiO_2 substrates and measured before deposition on actual devices. The test sample T_c is approximately 13 K.

Transport Measurements:

The data presented was measured utilizing a standard four-terminal lock-in technique. A low-frequency AC voltage generated by a lock-in amplifier is converted to an AC current using a large series resistor (1-10 M Ω) and the corresponding AC voltages (both NbN/g/Au and Au/g/Au channels) are measured at the same AC frequency along the sample. The current is sourced from the outer most Au electrode and drained into the NbN electrode. For equilibrium transport measurements (low excitation currents), when the system is in the Ohmic regime, $R = \frac{V_{AC}}{I_{AC}}$, where I_{AC} is the measured AC current and V_{AC} is the corresponding AC voltage. For non-equilibrium measurements, a DC+AC current bias scheme is used in which we superimpose a DC current bias I_{DC} onto the AC current excitation. The total current in such setup is: $I_{tot} = I_{AC} + I_{DC}$. This is achieved by connecting the source lock-in amplifier in parallel with a DC voltage source. A 10 M Ω resistor is placed after the lock-in output and a 100 k Ω resistor is placed after the DC voltage source output. The AC current is measured with a lock-in at the AC source frequency and the DC current is measured with the DC voltage source. In this configuration V_{AC} is a measurement of the differential resistance $R_{AC} = \frac{V_{AC}}{I_{AC}} = \frac{dV}{dI}$. An AC current excitation of ≈ 100 nA is used for all measurements.

Fitting Zero-Field NbN/g/Au Junction Conductance to BTK Theory:

To model the DC current dependence of the NbN/g/Au junction conductance in the RAR regime ($\epsilon_F > \Delta_{\text{NbN}}$), we use Blonder-Tinkham-Klapwijk theory¹. The total current across the NbN/g interface is proportional to $1 + R(E) + AR(E)$ which is the incident electron probability minus the reflected electron probability $R(E)$ plus the Andreev reflection probability $AR(E)$. The total current can be calculated by integrating the total electron probability over all available electronic states, which is modeled by Fermi functions. We assume the graphene has a chemical potential of $\mu_g = eV$ and the NbN is grounded $\mu_{\text{NbN}} = 0$.

$$\frac{I_{NS}(V)}{I_{NN}} = \frac{1 + Z^2}{V} \int_{-\infty}^{\infty} [f(E - eV, T) - f(E, T)](1 + AR(E) - R(E))dE \quad (S1)$$

Where I_{NS} is the current through the NbN/g/Au junction when the NbN is superconducting and I_{NN} is the current through the NbN/g/Au junction when the NbN is a normal metal. In our measurement in figure 1E, the sample temperature is much lower than the superconducting gap of NbN, so we can simplify equation (S1) taking the limit of $T \rightarrow 0$,

$$\frac{I_{NS}(V)}{I_{NN}} = \frac{1 + Z^2}{V} (1 + AR(eV) - R(eV)) V \quad (S2)$$

To compare the theory more directly to our experiment, we use equation (S2) to determine the differential conductance normalized to the normal state conductance.

$$\frac{G_{NS}(V)}{G_{NN}} = \frac{d}{dV} I_{NS}(V) \cdot R_{NN} = (1 + Z^2)[1 + AR(eV) - R(eV)] \quad (S3)$$

The original BTK derivation omits the role of energy broadening in the density of states. We can easily include the role of broadening by introducing a finite quasiparticle scattering lifetime $\frac{1}{\Gamma}$ and substituting $E \rightarrow E + i\Gamma$ in the expression for $R(E)$ and $AR(E)$ ¹.

Modeling NbN/g/Au Junction Conductance in the QH Regime:

In the quantum Hall regime, we use the Büttiker formalism to calculate the SC/g junction conductance. We expect the contribution to the conductance from Andreev processes to be a summation of available Andreev bound states crossing the Fermi level:

$$G_{AR} = \frac{e^2}{\pi\hbar} \sum_1^{n^*} B_n \quad (S4)$$

B_n is the hole probability. For this work, we focus specifically on the $\nu = 4$ quantum Hall state in which the conductance can be simplified to:

$$G_{AR} = \frac{e^2}{\pi\hbar} \sum_1^4 B_n = \frac{2e^2}{\pi\hbar} \frac{q^2/(1 - \gamma_0^2)}{1 + \sqrt{1 - q^2/(1 - \gamma_0^2)}} \quad (S5)$$

$q = \frac{2s}{(s^2 + w^2 + 1)}$ and $\gamma_0 = \frac{[s^2 + w^2 - 1] \sin(\frac{\pi\nu}{2}) + 2w \cos(\frac{\pi\nu}{2})}{s^2 + w^2 + 1}$. The interfacial scattering parameter is

defined as $w = \left[\frac{2m_N U_0^2}{\hbar^2 \epsilon_F^{(N)}} \right]^{\frac{1}{2}}$ (where m_N is the electron mass, U_0 is the interfacial scattering potential, and ϵ_F is the Fermi level of graphene) and the Fermi velocity mismatch parameter is $s = [\epsilon_F^{(S)} m_N] / [\epsilon_F^{(N)} m_S]$. In the main text, we extract the scattering parameter w from our data through the following procedure:

- (1) Extract minimum conductance within the $\nu = 4$ plateau and determine the hole probability B_n using equation (S4).

(2) Using equation (S5), we can determine w from the hole probability B_n (figure S11A).

To understand the field dependence of w , we need only examine the field dependence of the cyclotron frequency $\omega_c = \frac{eB}{mc}$. As perpendicular field increases, the cyclotron frequency increases. For a given filling factor $\nu = 2\varepsilon_F^{(N)}/(\hbar\omega_c)$, $\varepsilon_F^{(N)}$ is larger at higher fields due to the larger cyclotron motion frequency, resulting in smaller w at higher magnetic fields (figure S11B).

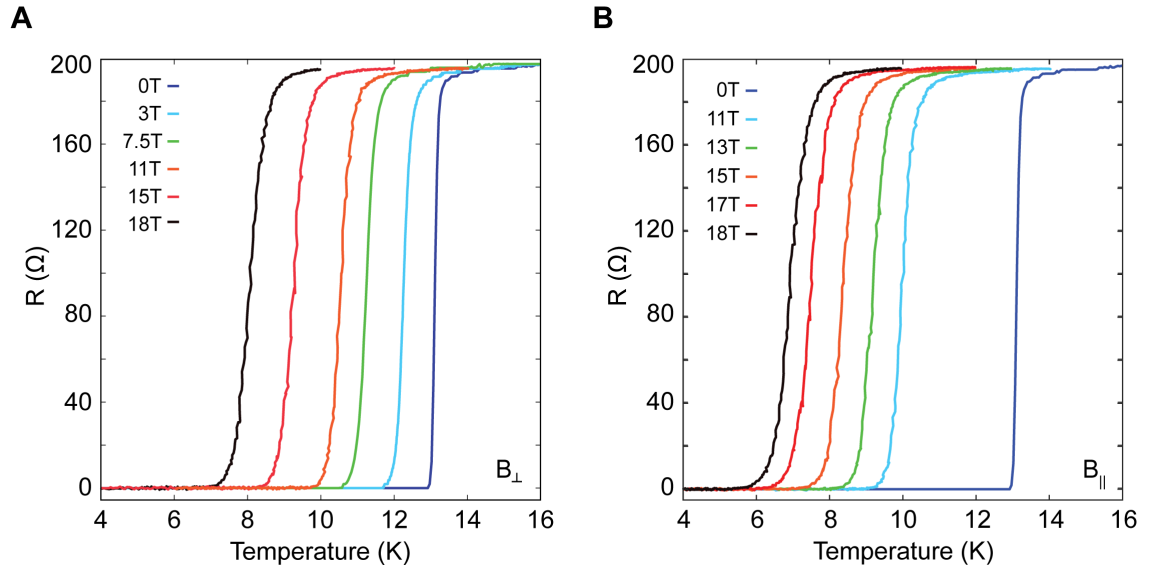


Figure S1. Superconducting properties of NbN. A,B) 4-terminal longitudinal NbN resistance versus temperature for various magnetic fields perpendicular (A) and parallel (B) to the sample plane. Results are consistent with expectations from supplemental reference².

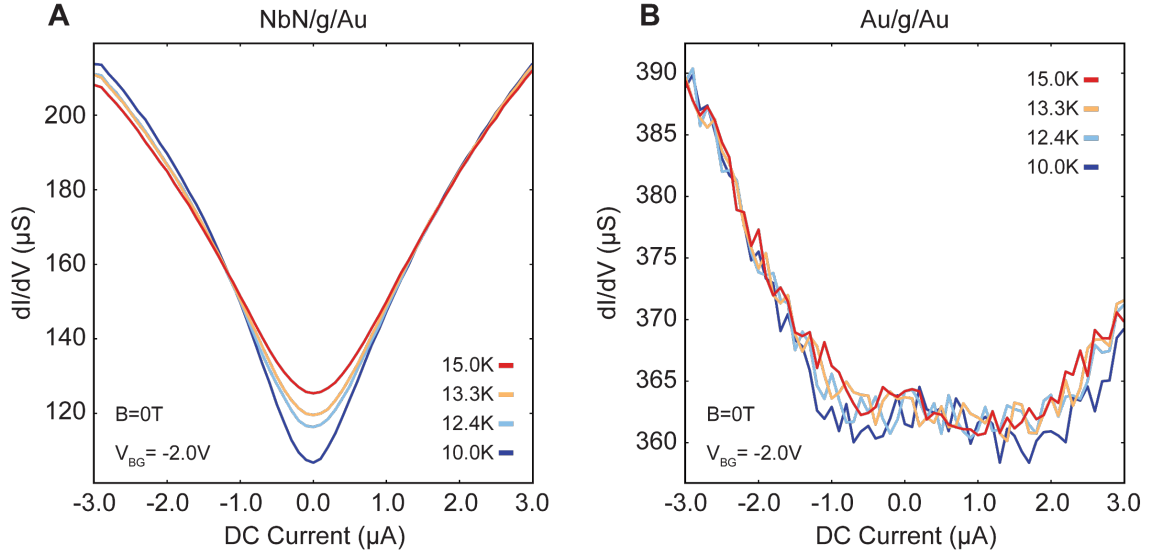


Figure S2. Temperature dependence of NbN/g/Au and Au/g/Au channel conductances. Differential NbN/g/Au (A) and Au/g/Au channel (B) conductance versus DC current bias for various temperatures across the NbN superconducting transition temperature ($T_C \approx 13.2$ K). The Au/g/Au channel is temperature independent across T_C , whereas the NbN/g/Au channel develops a zero-bias conductance dip and an increase in conductance for large biases for $T < T_C$ due to the emergence of Andreev reflection processes^{3,4}.

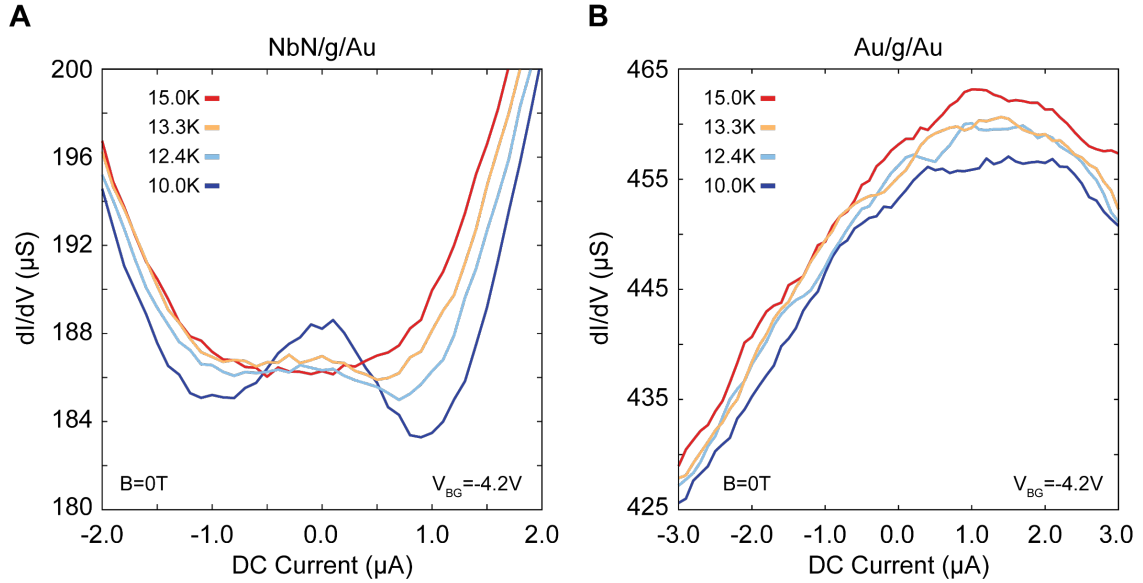


Figure S3. Temperature dependence of NbN/g/Au and Au/g/Au channel conductances. Differential NbN/g/Au (A) and Au/g/Au channel (B) conductance versus DC current bias for various temperatures across the NbN superconducting transition temperature ($T_C \approx 13.2$ K). The Au/g/Au channel is temperature independent across T_C , whereas the NbN/g/Au channel develops a zero-bias conductance peak for $T < T_C$ due to the emergence of Andreev reflection processes^{3,4}.

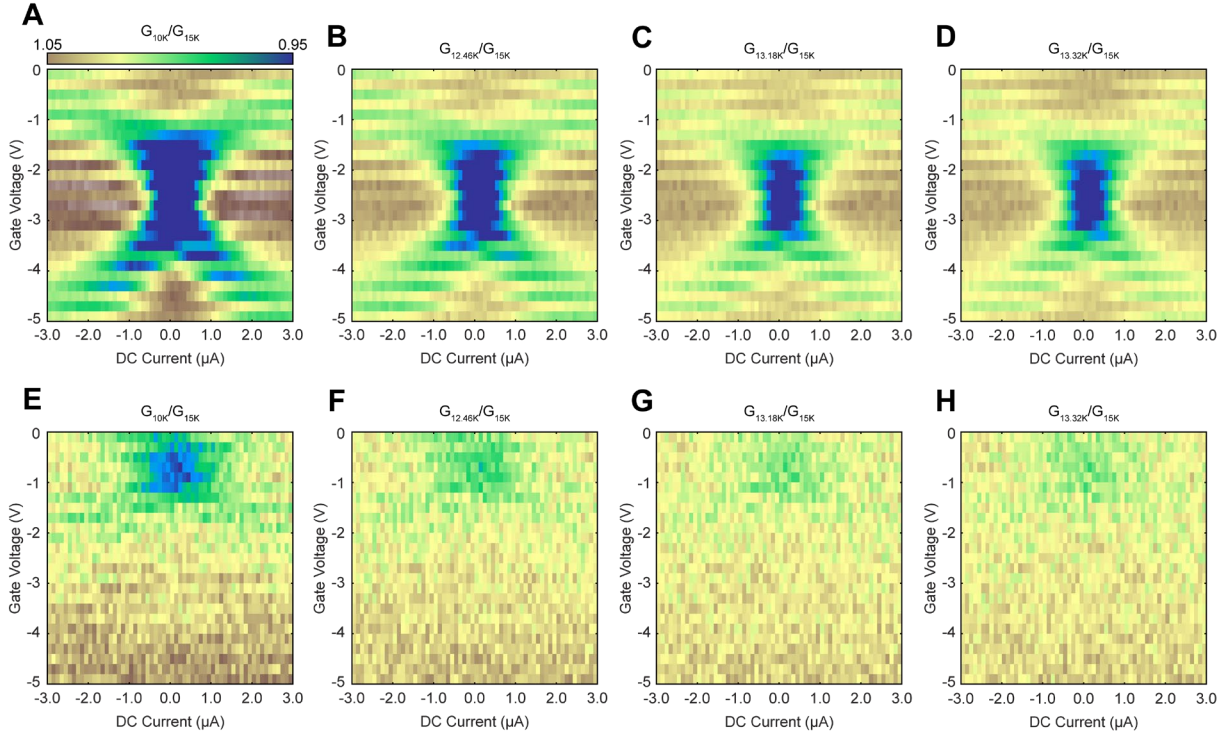


Figure S4. NbN/g/Au and Au/g/Au channel conductance maps across T_C . A-D) 2D color maps of differential NbN/g/Au channel conductance versus DC bias and back-gate voltage at 10 K (A), 12.46 K (B), 13.16 K (C), and 13.32 K (D). Each 2D color map is normalized by the 2D map taken at 15 K. The conductance enhancement at finite bias near the CNP (specular Andreev reflections) and the “cross” shaped feature become more prominent as temperature is lowered below the T_C of NbN^{3,4}. E-H) 2D color maps of differential Au/g/Au channel conductance versus DC bias and back-gate voltage at 10 K (E), 12.46 K (F), 13.16 K (G), and 13.32 K (H). Each 2D color map is normalized by the 2D map taken at 15 K.

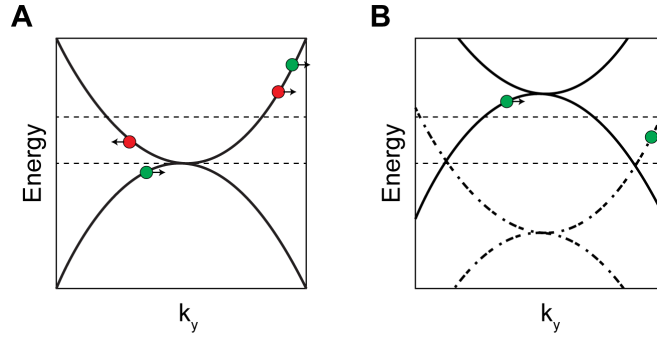


Figure S5. Specular Andreev reflection at zero bias. A) Cartoon of Andreev reflection processes at zero magnetic field. The graphene band structure is shown by the solid black lines. The two points in red correspond to intraband (retro) Andreev reflection processes, while the two points in green correspond to interband (specular) Andreev reflection processes. B) Cartoon of Andreev reflection processes at a finite parallel magnetic field. The dispersion for up-spin (solid black lines) and down-spin (dotted black lines) have the CNP's well separated energetically. Interband Andreev processes can occur at zero applied bias⁵. In both plots, dashed black lines denote the chemical potential and zero-field CNP.

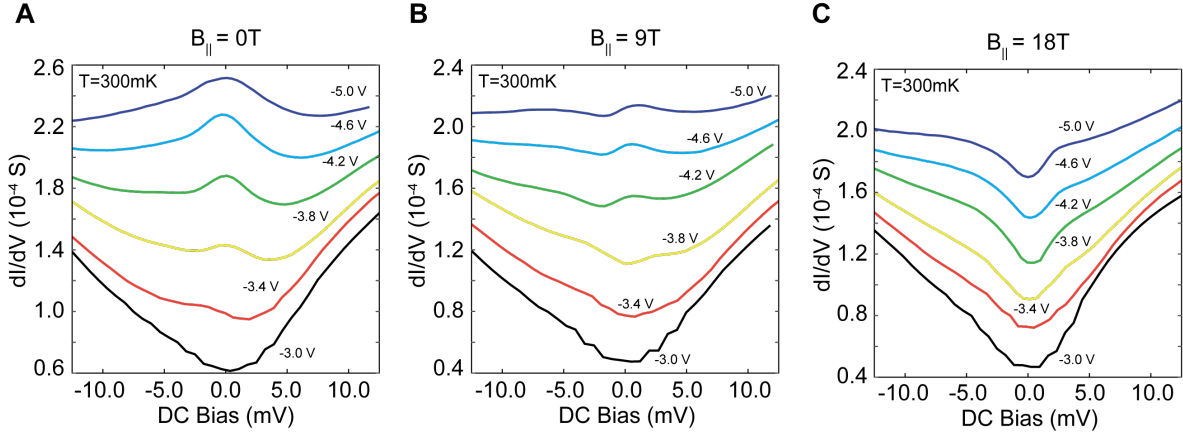


Figure S6. Elimination of conductance features with parallel magnetic field. Differential NbN/g/Au conductance versus DC voltage bias at various back-gate voltages for 0 T (A), 9 T (B), and 18 T (C) parallel magnetic fields. At zero magnetic field, as the back-gate voltage is swept away from the CNP, we observe three distinct tunneling regimes. At $V_{BG} = -3.0$ V, the Fermi level of graphene is at the CNP, manifesting a conductance dip near zero bias. At $V_{BG} = -4.2$ V, a zero-bias conductance peak emerges due to Andreev processes saddled by conductance minima corresponding to the condition where $e|V_{NS}| = \epsilon_F$. At $V_{BG} = -5.0$ V, the conductance minima disappear as the CNP is outside of the NbN superconducting gap and the graphene acts as a normal metal. As parallel magnetic field is increased, the conductance dips and zero-bias peaks disappear for any back-gate voltage due to Zeeman splitting of the graphene band structure⁵ and a reduction of the superconducting gap of NbN. To determine Zeeman splitting in the bilayer graphene, we extract the relative positions of conductance dips for a given V_{BG} at different fields: e.g. at $V_{BG} = -4.2$ V, the conductance dips move from ≈ 4.7 meV at 0 T, to ≈ 4.2 meV at 4.5 T to ≈ 3.6 meV at 9 T. This corresponds to a ≈ 1.1 meV Zeeman shift induced by 9 T parallel field, which gives a g factor ≈ 2.1 .

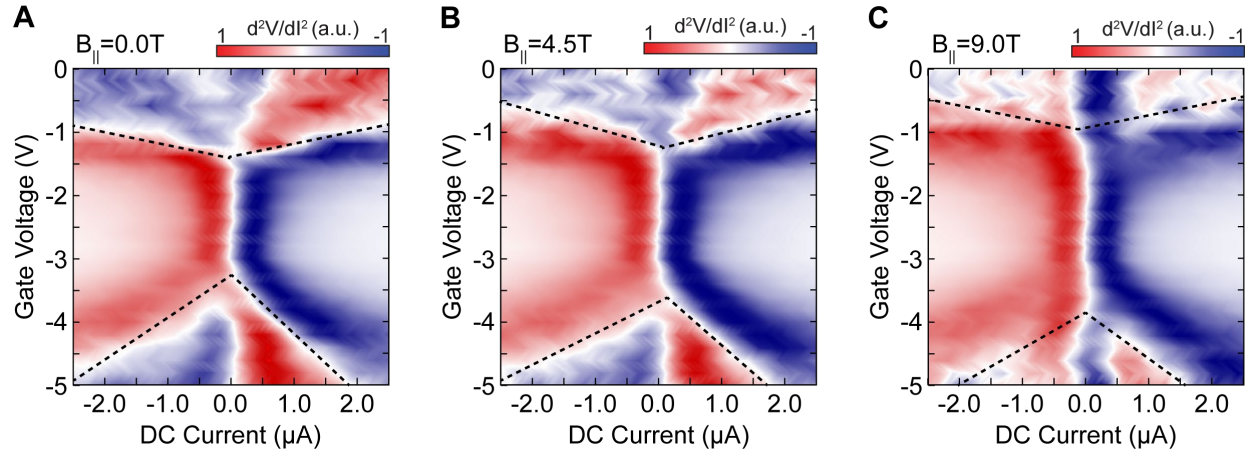


Figure S7. Movement of the RAR/SAR boundary with parallel magnetic field. Derivative of junction resistance versus back-gate voltage and DC current bias for 0 T (A), 4.5 T (B), and 9.0 T (C) parallel magnetic fields. The boundary between RAR and SAR processes are denoted by black dashed lines^{3,4}. At zero magnetic field, the position of the RAR/SAR crossover at zero DC bias is proportional to the disorder broadening in the NbN/g junction as the crossovers should intersect at the CNP. At finite fields, the position of the RAR/SAR crossover broadens due to the spin splitting of the graphene band structure⁵.

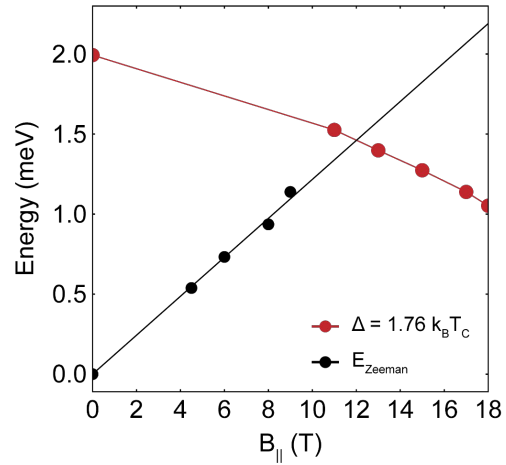


Figure S8. Evolution of Zeeman energy and NbN superconducting gap versus parallel magnetic field. Calculation of the superconducting gap of NbN (red dots and solid red line) and the extracted Zeeman splitting in bilayer graphene (black dots) and the corresponding fit (solid black line) versus parallel magnetic field. The bilayer graphene Zeeman splitting becomes larger than the superconducting gap of NbN at ~ 12 T.

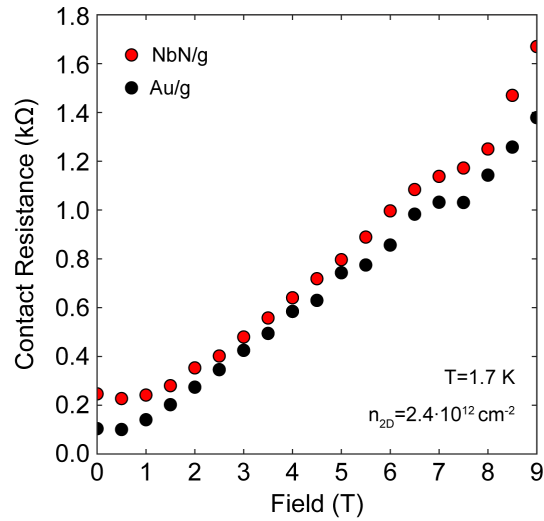


Figure S9. Contact resistances versus perpendicular magnetic field. NbN/g (red dots) and Au/g (black dots) contact resistances versus perpendicular magnetic field. The contact resistances are determined by measuring the 2-terminal NbN/g/Au and Au/g/Au resistances at a graphene density of $n_{2D} = 2.4 \cdot 10^{12} \text{ cm}^{-2}$ and subtracting the fridge line resistances. Contact resistances were extracted at 1.7 K.

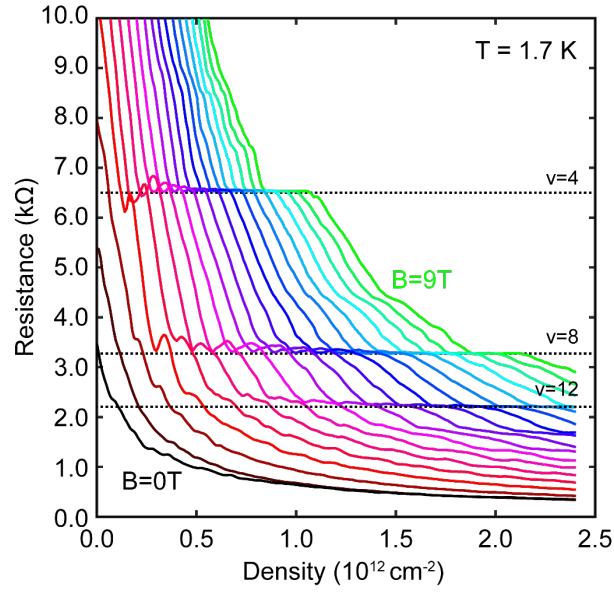


Figure S10. Fan diagram of the graphene channel. Au/g/Au channel resistance versus electronic carrier density at various magnetic fields. Observed well-quantized quantum Hall plateaus are denoted by dashed black lines.

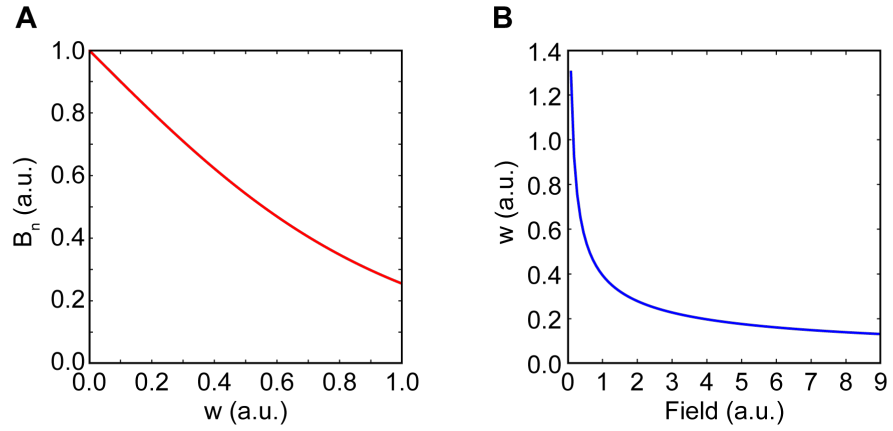


Figure S11. Calculation of SC/g interface parameters. A) Calculated hole probability B_n versus scattering parameter w assuming $s = 1$. B) Scattering parameter w versus magnetic field. All calculations were done using equations derived in reference⁶.

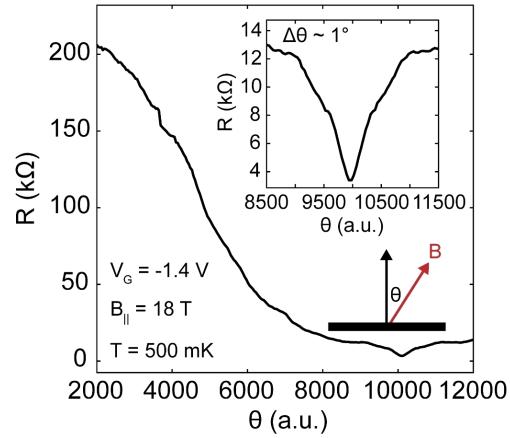


Figure S12. Calibrating the magnetic field direction. Resistance of the Au/g/Au channel versus sample rotator angle at 18 T and 500 mK with an applied back-gate voltage of -1.4 V (near the CNP). Inset shows a zoom in of the Au/g/Au channel resistance versus angle near 90° . The graphene resistance is minimized (maximized) when the magnetic field is oriented along the in-plane (out-of-plane) direction.

Supplemental References:

- (1) Blonder, G. E.; Tinkham, M.; Klapwijk, T. M. Transition from Metallic to Tunneling Regimes in Superconducting Microconstrictions: Excess Current, Charge Imbalance, and Supercurrent Conversion. *Phys. Rev. B* **1982**, *25* (7), 4515–4532. <https://doi.org/10.1103/PhysRevB.25.4515>.
- (2) Mondal, M.; Chand, M.; Kamlapure, A.; Jesudasan, J.; Bagwe, V. C.; Kumar, S.; Saraswat, G.; Tripathi, V.; Raychaudhuri, P. Phase Diagram and Upper Critical Field of Homogeneously Disordered Epitaxial 3-Dimensional NbN Films. *J. Supercond. Nov. Magn.* **2011**, *24* (1–2), 341–344. <https://doi.org/10.1007/s10948-010-1038-8>.
- (3) Efetov, D. K.; Efetov, K. B. Crossover from Retro to Specular Andreev Reflections in Bilayer Graphene. *Phys. Rev. B* **2016**, *94* (7), 075403. <https://doi.org/10.1103/PhysRevB.94.075403>.
- (4) Efetov, D. K.; Wang, L.; Handschin, C.; Efetov, K. B.; Shuang, J.; Cava, R.; Taniguchi, T.; Watanabe, K.; Hone, J.; Dean, C. R.; Kim, P. Specular Interband Andreev Reflections at van Der Waals Interfaces between Graphene and NbSe₂. *Nat. Phys.* **2016**, *12* (4), 328–332. <https://doi.org/10.1038/nphys3583>.
- (5) Soori, A.; Sahu, M. R.; Das, A.; Mukerjee, S. Enhanced Specular Andreev Reflection in Bilayer Graphene. *Phys. Rev. B* **2018**, *98* (7), 075301. <https://doi.org/10.1103/PhysRevB.98.075301>.
- (6) Hoppe, H.; Zülicke, U.; Schön, G. Andreev Reflection in Strong Magnetic Fields. *Phys. Rev. Lett.* **2000**, *84* (8), 1804–1807. <https://doi.org/10.1103/PhysRevLett.84.1804>.

Graphical TOC Entry

